Synthesis of Metal Oxide Microparticles for Use as Carriers of Intentional Forensic Signatures

James Louis-Jean[1*], Rachel Bergin[1], Michael Bronikowski[1], Wendy Kuhne[1], Seth Lawson[1], Abigail Waldron[1], Matthew Wellons[1], Spencer M. Scott[1]

[1]Savannah River National Laboratory, Aiken SC

Abstract

The trafficking of illicit and counterfeit materials is a far-reaching problem with significant economic impacts. The development and commercialization of taggant technologies, which can be introduced intentionally into commodity products to trace fraud or diversion through the rapid determination of commodity provenance, has received considerable interest within the context of forensics as a key deterrence strategy. Among the candidate taggant technologies, engineered microparticles (EµPs) offer a promising route for the introduction of intentional forensic signatures due to their highly uniform and tailorable physical and compositional properties. Taggant EµPs are a promising strategy for identifying the provenance of high consequence commodities such as nuclear material, including reactor fuel. Spray drying-based methods offer a facile and scalable route for the synthesis of EµPs with uniform composition, morphology, and particle size distribution. This work investigates the suitability of aerosol-based methods for the manufacture of taggant EµPs using the Savannah River National Laboratory (SRNL)-developed THermally Evaporated Spray for Engineered Uniform particulateS (THESEUS) system. In this system, uniform droplets of a feedstock solution containing a metal ion of the desired final composition are aerosolized, carried through a tube furnace (up to 1000 °C) for drying and oxide conversion, and collected using an electrostatic precipitator. Metal oxides of early candidate taggants for nuclear fuel (Mo and W) were used as an initial demonstration for the synthesis of taggant EµPs. The uniformity of the generated particles of MoO_3 and WO_3 were assessed using both *in situ* aerodynamic particle sizing measurements, as well as *ex-situ* automated particle analysis using scanning electron microscopy (SEM). The generated particles displayed highly uniform particle size distributions, with geometric standard deviations (σ_G) below 1.25. The material phase of the generated particles was confirmed using a combination of X-ray diffraction and Raman spectroscopy. This work demonstrates a facile route for the manufacture of particles with tailored physical and chemical properties for potential use as taggants in the nuclear fuel cycle.

Introduction

Counterfeiting and illicit trafficking of high-value products present an ongoing problem with significant economic and security impacts. As this challenge persists across industries and throughout global supply chains, there is a need to develop technologies to aid in the discrimination of counterfeit and genuine products and to identify diversion in supply chains. One proposed technique to accomplish this involves the use of taggants. Taggants are markers which can be incorporated into products to provide a means to establish provenance throughout the life cycle of a product, enabling the assessment of material provenance with high confidence.

Numerous methods for the encoding of taggant signatures have been proposed, including optical barcodes, novel chemical complexes and/or ratios, fluorescent additives, nanocrystalline inclusions, DNA barcodes, and isotopic barcodes.[1-3] Each of the proposed tagging mechanisms present unique tradeoffs involving their respective resolving power and/or discernability, ease and/or speed of taggant interpretation, resistance to adulteration, technical maturity, and cost to

implement. One proposed method for the introduction of taggants to a product or supply chain involves the use of highly uniform engineered microparticulates (EµPs) with tailored size, material phase, or isotopic composition, in which each particle serves as a carrier of the necessary information to identify the product's origins.[1]

This work investigates the synthesis of EµPs via an aerosol-based technique for use as taggants, specifically for nuclear fuel. EµPs offer a facile route for the introduction of taggants for which the taggant signatures are expected to be difficult to obfuscate given the pervasive nature of microparticulates and the sophistication of particle analysis techniques employed in fields such as nuclear safeguards and forensics.[4-6] Candidate taggant elements for nuclear fuel include tungsten and molybdenum, based on factors including the material compatibility with uranium oxide, material properties (i.e., melting temperatures), the number of stable isotopes, neutron absorption cross-sections, and the maturity of analytical techniques including mass spectrometry.[7-9] Aerosol-based techniques, such as spray drying or spray pyrolysis offer a scalable route for the manufacture of uniform particles with controllable properties such as size, morphology, and material phase, each of which may be further used to encode taggant information.[10] Spray drying techniques have been previously employed in the synthesis of tungsten oxide[11-13] and molybdenum oxide[14-16] particles.

This work leverages recent advances in the Savannah River National Laboratory (SRNL)-developed THermally Evaporated Spray for Engineered Uniform particulateS (THESEUS) system,[17, 18] developed for the manufacture of microparticulates with uniform size, material phase, and elemental and isotopic composition, to synthesize uniform particulates of tungsten trioxide (WO_3) and molybdenum trioxide (MoO_3). The demonstrated synthesis capability for uniform taggant particulates with controlled physical and compositional properties will be further explored as a route for the introduction of intentional forensic signatures into nuclear fuel, namely isotopic barcodes.

Experimental Methods

Material Feedstock Preparation

Feedstock solution of molybdic acid (Alfa Aesar CAS #7782-91-4, Lot #10224188, 85-90% purity) was prepared by dissolving the material in ultrapure water at room temperature, while tungstic acid (Alfa Aesar CAS #7783-03-1, Lot #P25F006, 99% purity) solution was prepared using a mixture of 30% H_2O_2 and ultrapure water at 45 °C for 30 min to promote dissolution. The desired feedstock solution concentrations (**Table 1**) were based on target calcined particle size as calculated using the Flow Focusing Monodisperse Aerosol Generator (FMAG, Model 1520, TSI Inc.) calculator provided by TSI, Inc. Manipulations were conducted using calibrated analytical balances and pipets, with nominal measurement errors of ±0.05 mg and ±0.001 mL, respectively.

Table 1. THESEUS operating conditions for EμPs taggants production under constant frequency, solution flow rate, dilution air flow, and flow focusing air pressure.

Feedstock	Conc. (vol/vol)	Target diameter (μm)	Temp (°C)	Target phase
$H_2MoO_4 \cdot xH_2O$	1.62E-4	1.0	700	MoO_3
$H_2WO_4 \cdot xH_2O$	1.25E-4	1.0	800	WO_3

THESEUS Particle Production

EμPs of MoO_3 and WO_3 were produced using the THESEUS system (**Figure 1**).[17, 18] Droplets of the feedstock solutions were generated via the FMAG at a frequency of 150 kHz with a solution injection rate of 3 mL/h, and a flow-focusing pressure of 2.00 ± 0.05 psi. Filtered air, at a flow rate of 10.0 ± 0.1 L/min was used as a carrier of the aerosolized droplets through the system. The droplets were thermally converted to the desired oxide phases (**Table 1**) via inline heating using a tube furnace (Model TF55030C-1, Thermo Fisher Scientific, Inc.) equipped with a 1-inch Inconel 625 tube. The generated particles were collected via an SRNL-designed electrostatic precipitator (ESP)[19] on polished silicon and carbon planchets for small scale (μg) production or onto electropolished stainless steel plates for milligram-scale powder production. An Aerodynamic Particle Sizer (APS, Model 3321, TSI Inc.) was used to measure *in situ* particle size distributions and assess stability of the system during sustained (multi-day) operations involved in the generation of milligram-scale powder production.
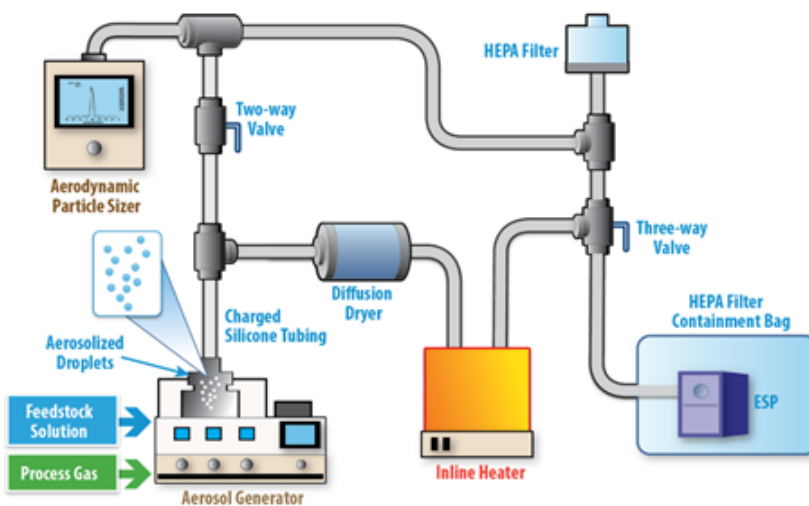
Figure 1. Schematic representation of the THermally Evaporated Spray for Engineered Uniform particulateS (THESEUS) system. Aerosol are formed via the generator, dried, calcined, and collected downstream via ESP.

Characterization

Powder X-ray diffraction (PXRD) measurements were performed at room temperature using Cu Kα X-rays (1.5406 Å). Individual particles were characterized using the Renishaw InVia Raman spectrometer, analyzed with a 514 nm laser, 1800 gv/mm grating, and the 1-inch CCD (UV – enhanced deep depletion CCD detector, cooled to -70 °C). The particles were viewed under a 100x microscope objective with a 30 s exposure time. Acquisitions were static, centered around 1000 cm^{-1}, giving a range of around 25-1900 cm^{-1}. Power flux studies were completed to evaluate the effect of laser power on particle oxidation with laser intensity controlled by neutral density filters

to values of 1, 2.5, 5, and 10% power. Based on preliminary characterizations, 2.5 and 5 % power were selected to avoid damage and total ablation of particles. Raman spectra of multiple particles per sample were subsequently processed in Wire 5.1 software for background subtraction and Origin for smoothing.

High-resolution scanning electron microscopy (SEM) measurements were collected using a field emission Tescan Mira 4 (Model S6122) with an accelerating voltage of 5 keV as well as a field emission Carl Zeiss Supra 40VP SEM operated by Zeiss SmartSEM and equipped with an Oxford X-Max 80 mm^2 detector using Oxford AzTEC software. Automated Particle Measurement (APM) identified particle morphology by signal intensity and elemental composition using energy-dispersive X-ray (EDX) with an accelerating voltage of 20 keV. Reconciliation of APS and APM size distributions was used to estimate the apparent density of the particles by applying an inverse square of density with a shape correction factor of one to the APS data.

Results

Aerodynamic Sizing and Electron Microscopy Characterization

The short residence time in the furnace (0.93 s) and thermal processing of the feedstock material to stable oxide induced noticeable morphological features on the surface of MoO_3 and WO_3 EµPs, as shown in **Figure 2** and **Figure 3**, respectively. Other well-defined parameters showed significant compositional dependence between particle type including aerodynamic size, geometric standard deviations (σ_G), and density (**Table 2**). Both MoO_3 and WO_3 EµPs formed highly spherical particles with monodisperse size distributions, as evidenced by σ_G values below 1.25 in the APS, though MoO_3 particles via SEM exhibited a larger σ_G value. The average ECD was larger than target 1 µm for both particle types (**Table 1**). Correspondingly, the apparent density of these EµPs also fell below value; this is hypothesized as the result of increased porosity and other morphological inconsistencies in particle production.

Table 2. Particulates size comparison of as-generated EµPs taggants along with their associated geometric standard deviation and corrected particle density.

EµP phase	APS		SEM		Density	
	Aerodynamic size (µm)	Geometric Standard Deviation (σ_G)	APM Average ECD (µm)	Geometric Standard Deviation (σ_G)	Theoretical (g/cm^3)	Calculated (g/cm^3)
MoO_3	2.20	1.10	1.45	1.33	4.71	2.32
WO_3	3.11	1.07	1.55	1.25	7.15	4.01

Note: σ_G is unitless; ≤ 1.25 indicates monodisperse and > 1.25 indicates polydisperse aerosol size distribution.

The generated MoO_3 particles have a spherical to spheroidal morphology which exhibit a broad particle size distribution spanning the range of approximately 1-2 µm as displayed by APS and APM-SEM (**Figure 2**). The microporous nature of these particles is hypothesized as resulting from the rapid dehydration of the uniform aerosolized droplet of the feedstock within the furnace, followed by phase transition during sintering of solid particles to yield highly crystalline MoO_3 EµPs. Concurrent formation of different MoO_3 phases could also impact the apparent morphology and density of EµPs. The observed particle porosity, morphological inconsistency and size

distribution of MoO_3 correlates to a reduced particle density (2.32 g/cm^3) compared to that expected (4.71 g/cm^3).[20] This decrease in density resulted in larger than anticipated particle size.
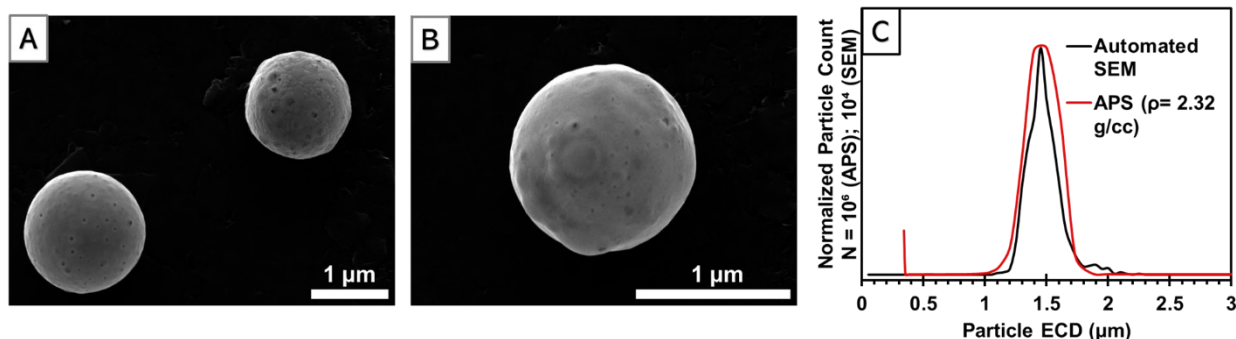
Figure 2. SEM images (A) and (B) of representative MoO_3 particles and particle size comparison (C) by APS and APM-SEM consolidation.

While the WO_3 EµPs were produced as uniform spherical particles and as confirmed by their σ_G value, two distinct particulate morphologies were observed within their population. Based on SEM image analysis, the rough textured surface observed on some of the particles, likely the result of rapid dehydration of the aerosolized tungstic acid feedstock, did not produce a noticeable change in particle diameter compared to the smooth spherical particles (**Figure 3**). Calculated density of generated WO_3 EµPs is estimated as 4.01 g/cm^3 from reconciliation of APS and APM-SEM particle size distributions (**Figure 3**), consistent with about 56.1% of theoretical density (7.15 g/cm^3) of bulk material.[21]
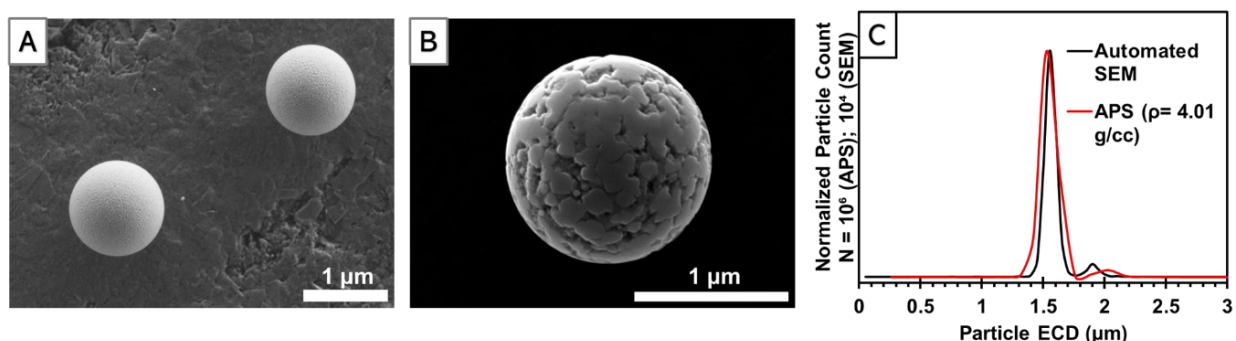
Figure 3. SEM images (A) and (B) of representative WO_3 particles and particle size comparison (C) by APS and APM-SEM consolidation.

Following initial synthesis of µg-scale particle production, effort to demonstrate the feasibility for mg-scale production of EµPs was undertaken, involving up to 30 hours of sustained operation of the THESEUS system using similar parameters as developed for planchet production. Particulate oxide materials were collected from the ESP and the theoretical production rates of MoO_3 and WO_3 EµPs were calculated as 3.73 and 2.28 mg/h, respectively.

During production, *in situ* APS measurements were collected to assess the stability of particle size and concentration. While this operation involved multi-day particulate batch production, MoO_3 and WO_3 particulates retained their spherical morphology, monodispersity, and relative particle sizes (**Figure 4**). This lab-scale production coupled with the uniformity of particulate size indicates promise for future scale-up.
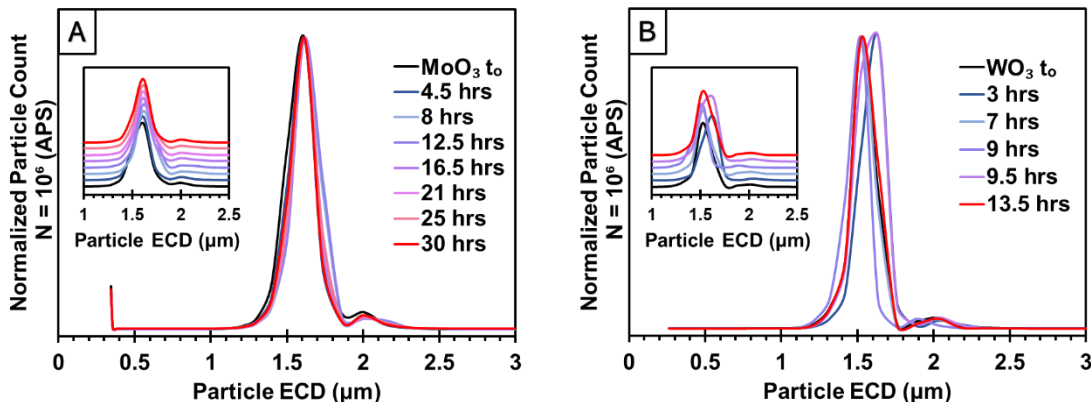
Figure 4. Aerodynamic size for mg-scale production of (A) MoO_3 over 30 hours and (B) WO_3 over 13.5 hours with stacked plot inserted for clarity.

X-ray Diffraction Characterization

Structural and phase characterizations of the MoO_3 and WO_3 particulates were studied using PXRD and Raman spectroscopy. The PXRD patterns of these EµPs are characterized as sharp detectable peaks indicating well-crystallized materials (**Figure 5**).
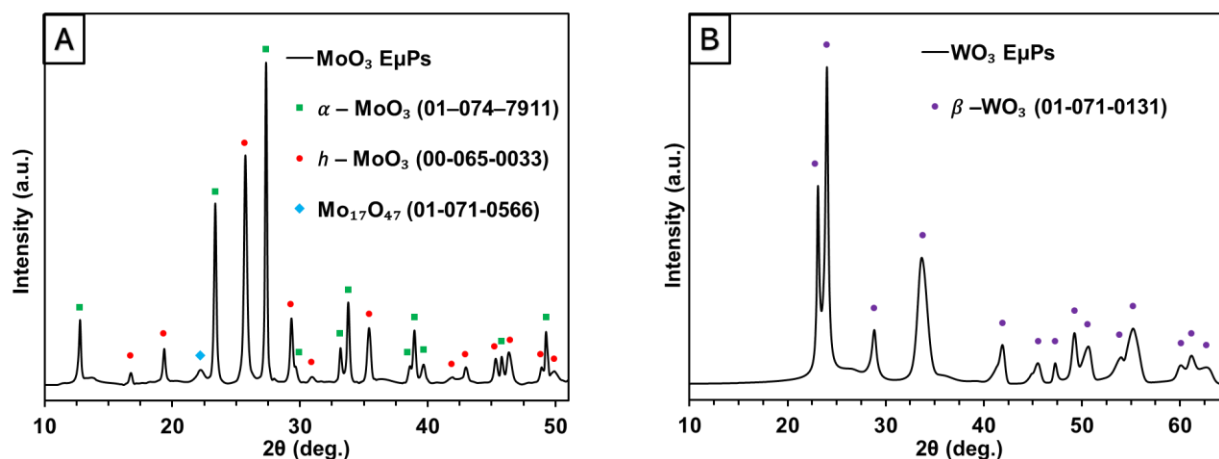
Figure 5. Powder XRD patterns of the synthesized (A) MoO_3 and (B) WO_3 particulates as indexed with their respective phases and corresponding powder diffraction files.

With the operating temperature (700 °C) of the furnace, α-MoO_3 phase should be expected to form. However, the PXRD pattern of molybdenum oxide EµPs indicates a mixture of the orthorhombic α-MoO_3 and hexagonal h-MoO_3 phases as well as a trace hypostoichiometric $MoO_{2.76}$ phase, (**Figure 5A**) which are induced by rapid calcination. The formation of α-MoO_3 from h-MoO_3 is known to irreversibly occur above 400 °C.[22] Mixed oxide phases (α- and h-MoO_3) and reduced species (Mo_4O_{11}, =$MoO_{2.75}$) have been previously observed during the production of molybdenum oxide particles using spray pyrolysis techniques as controlled by temperature and Mo feedstock concentration.[14]

The dehydration process for tungstic acid (800 °C) exceeded the temperature at which the tetragonal phase (α-WO_3) can form in bulk material, however each of the trioxide phases are formed by corner or edge shared WO_6 octahedral where the higher temperature phases (α-, β-WO_3) often relax toward the more stable and lower density monoclinic phase (γ-WO_3) during cooling to

6

room temperature.[23] Rather than α- or γ-WO₃ phases, the experimental PXRD pattern (**Figure 5B**) indicates the formation of a highly crystalline material whose pattern matches precisely with the orthorhombic (β-WO₃) phase, likely the result of rapid and nonequilibrium cooling.

The crystallinity of the EμPs was also investigated using both Scherrer and Williamson-Hall methods [24] while considering a shape factor of 1 and X-ray wavelength of 0.15406 nm for Cu k$_\alpha$. The crystallite size of these EμPs show relatively good agreement between methods, where MoO₃ crystallite sizes were estimated as 34.54 and 28.09 nm and those for WO₃ were estimated as 16.57 and 9.27 nm via the Scherrer and Williamson-Hall methods, respectively. The discrepancy observed is primarily due to lattice strain not considered in Scherrer formulation, meaning the Williamson-Hall method provides a better approach for the estimation of crystallite size. The increased crystallite size for MoO₃ can likely be attributed to the multiple phases present compared to the single WO₃ phase.

Raman Spectroscopy Characterization

The structures of the MoO₃ and WO₃ particulates were investigated by Raman spectroscopy (**Figure 6**) to identify their vibrational properties and phases in relation to their synthetic routes and PXRD characterizations. There were no significant differences observed between Raman spectra from different production campaigns of the same type of EμP, confirming the homogeneity of the crystal structures.
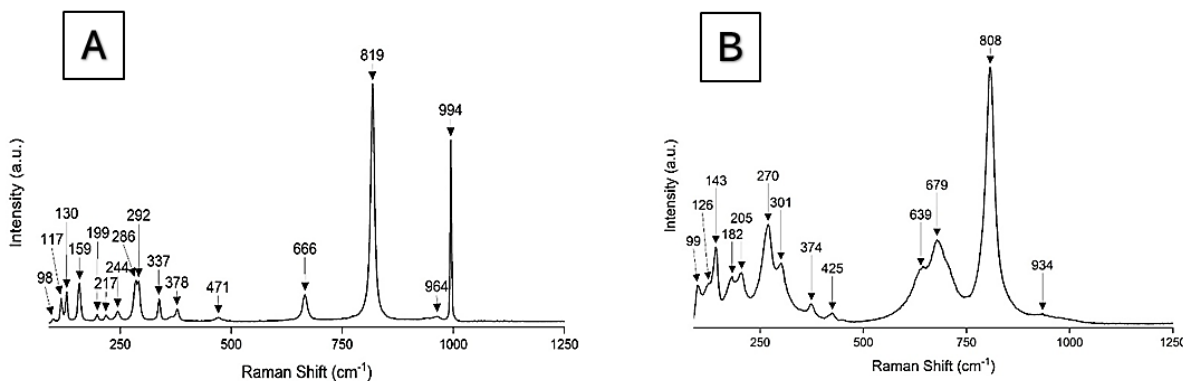
Figure 6. Single particle μ-Raman spectra of (A) MoO₃ and (B) and WO₃.

The Raman spectrum of MoO₃ EμPs (**Figure 6A**) exhibits well-defined Raman bands matching literature values – primarily for high crystalline α-MoO₃ (orthorhombic) materials.[25] The Raman bands at 994 cm^{-1} and 819 cm^{-1} are assigned to the asymmetric and symmetric stretching frequency of the Mo=O bonds, respectively, whereas the 666 cm^{-1} band is due to the asymmetric stretching of O–Mo–O. Additional Raman bands due to various lattice modes within the crystalline structure of MoO₃ EμPs occur at lower frequency. Of particular interest, the intensity ratio of the wagging modes of MoO₃ (O=Mo=O) as observed at 286 cm^{-1} and 292 cm^{-1} reflects a partially distorted structure due to oxygen deficiency.[26, 27] This observation further supports the experimental PXRD pattern for MoO₃ particulates.

The Raman spectrum of WO₃ EμPs (**Figure 6B**) also shows vibrational bands reflecting literature, where the bands between 630-810 cm^{-1} are attributed to either the antisymmetric stretching of W–O–W bonds or the symmetric stretching of O–W–O bonds and the weak (low intensity) band at 934 cm^{-1} is attributed to the vibration of terminal W=O bonds.[21, 28, 29] The lower frequency regions

in the spectrum occur due to various lattice modes which are consistent to orthorhombic WO_3 crystalline structure and as confirmed by the experimental PXRD pattern.

Conclusion

Highly uniform metal oxide EµPs with tailorable size were successfully manufactured using the SRNL-developed THESEUS system, with targeted applications including use as taggants within nuclear fuel. Good agreement was achieved between aerodynamic and automated SEM sizing measurements for the generated MoO_3 and WO_3 particles, indicating monodisperse particle populations, with geometric standard deviations (σ_G) below 1.25. This monodispersity indicates a high degree of compositional homogeneity, as evidenced by the results from PXRD and Raman analysis. Phases observed matched the predicted oxides of MoO_3 and WO_3, with MoO_3 presenting with multiple polymorphs and a trace hypostoichiometric phase. This observation of multiple, similar MoO_3 phases with variation in unit cell size is likely the cause of the decreased apparent density and the visible surface porosity. The ability to produce highly homogenous MoO_3 and WO_3 EµPs provides a foundation for the production of isotopically perturbed EµPs and will support ongoing and future investigations towards the application of isotopically-barcoded taggants within the nuclear fuel cycle.

References

1.   Paunescu, D.; Stark, W. J.; Grass, R. N., Particles with an identity: tracking and tracing in commodity products. *Powder technology* **2016,** *291*, 344-350.

2.   Müssig, S.; Reichstein, J.; Miller, F.; Mandel, K., Colorful Luminescent Magnetic Supraparticles: Expanding the Applicability, Information Capacity, and Security of Micrometer-Scaled Identification Taggants by Dual-Spectral Encoding. *Small* **2022,** *18*, (13), 2107511.

3.   Arppe, R.; Sørensen, T. J., Physical unclonable functions generated through chemical methods for anti-counterfeiting. *Nature Reviews Chemistry* **2017,** *1*, (4), 0031.

4.   Donohue, D.; Vogt, S.; Ciurapinski, A.; Ruedenauer, F.; Hedberg, M. *Particle analysis of environmental swipe samples*; IAEA-SM-367/10/07: 2001.

5.   Keegan, E.; Kristo, M. J.; Toole, K.; Kips, R.; Young, E., Nuclear forensics: scientific analysis supporting law enforcement and nuclear security investigations. In ACS Publications: 2016.

6.   Betti, M.; Tamborini, G.; Koch, L., Use of secondary ion mass spectrometry in nuclear forensic analysis for the characterization of plutonium and highly enriched uranium particles. *Analytical Chemistry* **1999,** *71*, (14), 2616-2622.

7.   LaMont, S.; Phillips, J.; Bedell, J.; Goorevich, R.; Nusbaum, D.; Karpas, Z.; Maimon, E.; Sadan, Y.; Reich, G. In *Use of chemical and isotopic tracers as part of an improved safeguards approach in uranium conversion facilities*, 8th International Conference on Facility Operations: Safeguards Interface 2008, 2008; 2008; pp 111-130.

8.   Wilson, B.; Shields, A.; Russell, N.; Nelson, A.; Ulrich, T.; Scott, S.; Wellons, M. *Irradiation of Isotopically Tagged UO2 Fuel for Intentional Forensics Purposes*; Oak Ridge National Lab.(ORNL), Oak Ridge, TN (United States): 2022.

9.   Kristo, M.; Robel, M.; Hutcheon, I. *Nuclear Forensics and Attribution for Improved Energy Security: The Use of Taggants in Nuclear Fuel*; Lawrence Livermore National Lab.(LLNL), Livermore, CA (United States): 2007.

10.   Messing, G. L.; Zhang, S. C.; Jayanthi, G. V., Ceramic powder synthesis by spray pyrolysis. *Journal of the American Ceramic Society* **1993,** *76*, (11), 2707-2726.

11.   Govender, M.; Shikwambana, L.; Mwakikunga, B. W.; Sideras-Haddad, E.; Erasmus, R. M.; Forbes, A., Formation of tungsten oxide nanostructures by laser pyrolysis: stars, fibres and spheres. *Nanoscale Research Letters* **2011,** *6*, (1), 166.

12.   Nakakura, S.; Arif, A. F.; Rinaldi, F. G.; Hirano, T.; Tanabe, E.; Balgis, R.; Ogi, T., Direct synthesis of highly crystalline single-phase hexagonal tungsten oxide nanorods by spray pyrolysis. *Advanced Powder Technology* **2019,** *30*, (1), 6-12.

13.   Nandiyanto, A. B. D.; Arutanti, O.; Ogi, T.; Iskandar, F.; Kim, T. O.; Okuyama, K., Synthesis of spherical macroporous WO3 particles and their high photocatalytic performance. *Chemical Engineering Science* **2013,** *101*, 523-532.

14.   Choi, H.; Kim, D.; Yoon, S. P.; Han, J.; Ha, S.; Kim, J., Production of molybdenum oxide particles with high yield by ultrasonic spray pyrolysis and their catalytic activity toward partial oxidation of n-dodecane. *Journal of Analytical and Applied Pyrolysis* **2015,** *112*, 276-283.

15.   Ding, Q. P.; Huang, H. B.; Duan, J. H.; Gong, J. F.; Yang, S. G.; Zhao, X. N.; Du, Y. W., Molybdenum trioxide nanostructures prepared by thermal oxidization of molybdenum. *Journal of Crystal Growth* **2006,** *294*, (2), 304-308.

16.   Kumar, V.; Wang, X.; Lee, P. S., Formation of hexagonal-molybdenum trioxide (h-MoO(3)) nanostructures and their pseudocapacitive behavior. *Nanoscale* **2015,** *7*, (27), 11777-86.

17.   Scott, S. M.; Baldwin, A. T.; Bronikowski, M. G.; II, M. A. D.; Inabinet, L. A.; Kuhne, W. W.; Naes, B. E.; Smith, R. J.; Eliel, V.-A.; Tenner, T. J.; Wurth, K. N.; Wellons, M. S., Scale-up And Production Of Uranium-bearing QC Reference Particulates By An Aerosol Synthesis Method. *Proceedings of the Joint INMM & ESARDA 2021 Meeting* **2021**.

18.   Benjamin E. Naes, S. S., Abigail Waldron, Seth Lawson, Michael G. Bronikowski, Laken A. Inabinet, Ross J. Smith, Kimberly N. Wurth, Travis J. Tenner and Matthew Wellons, Production of Mixed Element Actinide Reference Particulates to Support Nuclear Safeguards using THESEUS, an Aerosol-based Particulate Synthetic Methodology. *Under Review* **2023**.

19.   Carlson, D. C.; Degange, J. J.; Cable-Dunlap, P., Portable aerosol contaminant extractor. In Google Patents: 2005.

20.   Leisegang, T.; Levin, A.; Walter, J.; Meyer, D., In situ X-ray analysis of MoO3 reduction. *Crystal Research and Technology: Journal of Experimental and Industrial Crystallography* **2005,** *40*, (1-2), 95-105.

21.   Salje, E., The orthorhombic phase of WO3. *Acta Crystallographica Section B* **1977,** *33*, (2), 574-577.

22.   Ramana, C. V.; Atuchin, V. V.; Troitskaia, I. B.; Gromilov, S. A.; Kostrovsky, V. G.; Saupe, G. B., Low-temperature synthesis of morphology controlled metastable hexagonal molybdenum trioxide (MoO3). *Solid State Communications* **2009,** *149*, (1), 6-9.

23.   Zheng, H.; Ou, J. Z.; Strano, M. S.; Kaner, R. B.; Mitchell, A.; Kalantar-zadeh, K., Nanostructured tungsten oxide–properties, synthesis, and applications. *Advanced Functional Materials* **2011,** *21*, (12), 2175-2196.

24.   Cullity, B. D.; Stock, S. R., *Elements of X-ray Diffraction*. 3rd ed.; Pearson New International Edition: 2001.

25.   Silveira, J. V.; Vieira, L. L.; Filho, J. M.; Sampaio, A. J.; Alves, O. L.; Souza Filho, A. G., Temperature-dependent Raman spectroscopy study in MoO3 nanoribbons. *Journal of Raman spectroscopy* **2012,** *43*, (10), 1407-1412.

26.   Dieterle, M.; Weinberg, G.; Mestl, G., Raman spectroscopy of molybdenum oxides Part I. Structural characterization of oxygen defects in MoO 3− x by DR UV/VIS, Raman spectroscopy and X-ray diffraction. *Physical Chemistry Chemical Physics* **2002,** *4*, (5), 812-821.

27.   Mestl, G.; Srinivasan, T.; Knözinger, H., Mechanically activated MoO3. 3. Characterization by vibrational spectroscopy. *Langmuir* **1995,** *11*, (10), 3795-3804.

28.   Daniel, M. F.; Desbat, B.; Lassegues, J. C.; Gerand, B.; Figlarz, M., Infrared and Raman study of WO3 tungsten trioxides and WO3, xH2O tungsten trioxide tydrates. *Journal of Solid State Chemistry* **1987,** *67*, (2), 235-247.

29.   Gabrusenoks, J.; Veispals, A.; Czarnowski, A. v.; Meiwes-Broer, K. H., Infrared and Raman spectroscopy of WO3 and CdWO4. *Electrochimica Acta* **2001,** *46*, 2229-2231.